A model to predict image formation in the three-dimensional field ion microscope

Benjamin Klaes, Rodrigue Lardé, Fabien Delaroche, Stefan Parviainen, Nicolas Rolland, Shyam Katnagallu, Baptiste Gault, François Vurpillot

Version of Record: https://www.sciencedirect.com/science/article/pii/S0010465520301235
Manuscript_50b5489beb218898dd1ee4ca8b879097

A model to predict image formation in the three-dimensional field ion microscope

Benjamin Klaes[1], Rodrigue Larde[1], Fabien Delaroche[1], Stefan Parviainen[1], Nicolas Rolland[4], Shyam Katnagallu[2], Baptiste Gault[2,3], and François Vurpillot[1,2]

Corresponding Author: francois.vurpillot@univ-rouen.fr

1. Normandie Université, UNIROUEN, INSA Rouen, CNRS, Groupe de Physique des Matériaux, 76000 Rouen, France.
2. Department of Microstructure Physics and Alloy Design, Max-Planck-Institut für Eisenforschung GmbH, Max-Planck-Straße 1, 40237 Düsseldorf, Germany
3. Department of Materials, Royal School of Mines, Imperial College London, Prince Consort Road, London, SW7 2BP, United Kingdom
4. Laboratory of Organic Electronics, Department of Science and Technology (ITN), Campus Norrköping, Linköping University, SE-60174 Norrköping, Sweden

Abstract

Field ion microscopy (FIM) was the first technique to image individual atoms on the surface of a material. By a careful control of the field evaporation of surface atoms, the bulk of the material is exposed, and, through digital processing of a sequence of micrographs, an atomically-resolved three-dimensional reconstruction can be achieved. 3DFIM is particularly suited to the direct observation of crystalline defects that underpin the physical properties of materials: vacancies and vacancy clusters, interstitials, dislocations, or grain boundaries. Yet, further developments of 3DFIM are necessary to turn it into a routines technique. Here, we introduce first a protocol for 3DFIM image processing and subsequent tomographic reconstruction. Second, we propose a numerical model enabling simulation of the FIM imaging process. The model combines the meshless algorithm for field evaporation proposed by Rolland et al. (Robin-Rolland Model, or RRM) with fundamental aspects of the field ionization process of the gas image involved in FIM. The proposed model enables the simulation of imaging artefacts that are induced by non-regular field evaporation and by the disturbed electric field distribution near atomic defects. Our model enables more precise interpretation of 3DFIM characterization of structural defects.

Keywords : Field Ion Microscopy, Simulation, tomography, field evaporation, field ionisation

1. Introduction

Field ion microscopy (FIM) allows for direct imaging of the surface of a material with true atomic resolution. In a FIM experiment, a needle-shaped specimen is placed inside an ultra-high vacuum chamber, in which an imaging gas, such as neon or helium, is inserted at low pressure ($<10^{-3}$Pa). FIM relies on the ionization of these imaging gas atoms from prominent positions above the specimen's

surface, exploiting the effect of an intense electric field. The electric field is produced by subjecting a cryogenically-cooled (T<100K) specimen prepared as a sharply pointed needle to a high voltage (a few kV). When the radius of curvature at the needle's apex is sufficiently small (i.e. below 100nm), the very strong DC electric field enables direct ionization of the image gas in the vicinity of the surface. The specimen is placed in front of an imaging screen. The divergent surface electric field drives away the ions from the surface, creating a highly magnified projection of the atomic arrangement at the specimen's surface onto the screen. Each bright spot in FIM images is the result of tens of thousands of imaging gas ions projected onto the FIM screen every second. More details on the technique can be found in numerous textbooks [1–3] .

From the 1950s, and for the following two decades, FIM was established as the first true atomic-scale microscopy technique [4], achieving direct space imaging of the positions of individual atoms [5] with atomic precision [6]. The ability to localize precisely the 3-D coordinates of individual atoms in direct space is a major asset for materials science. For instance, early atomic-scale investigations of structural defects, such as vacancies and dislocations in metals[7–10], were enabled by FIM. The reconstruction of 3-D distribution of single vacancies caused by ion irradiation in W by FIM was the first of its kind [11,12].

The most difficult aspect of FIM studies is to efficiently retrieve the information contained within the collected images. FIM images must be carefully interpreted to obtain the positions of individual atoms in the 3-D real space. Additionally, special care must be taken to avoid misinterpretations and image distortions associated to e.g. surface diffusion [13] or artefacts of field-evaporation[14]. The dynamic aspect of the technique, where FIM images are snapshots of the specimen's surface at given steps of field evaporation, also complicate the interpretation. Successful attempts at reconstructing 3D volumes from FIM images have already been reported [15,16] and automated procedures were developed for the reconstruction of accurate 3D, lattice-resolved atom maps. These procedures rely on image processing techniques to detect the positions of hundreds of atoms within each micrograph. These atoms are then digitally track across a sequence of FIM images, from the moment when they are first revealed at the surface of the specimen to their field evaporation. Using the latest generation of graphic workstations, images extracted from FIM movies can thus be used to produce high resolution 3D reconstructions of the whole apex. This breakthrough theoretically qualifies FIM as the most precise available tool for the full tomographic real space imaging of atoms in bulk materials, in volumes larger than 100x100x100 nm^3. Nevertheless, to achieve this ultimate goal, the spatial performances of the technique (such as spatial resolution, accuracy, noise, efficiency…) must also be qualified on a theoretical basis.

To this aim, a preliminary model developed to interpret 3D reconstructed FIM images was recently developed [17]. It was shown that atomic positions reconstructed from FIM in a pure metal case (W) could be experimentally observed with systematic displacements of a maximum of 0.05 nm due to the change in the direction of the surface highest electric field caused by the field evaporation of neighbouring atoms. This was demonstrated by comparing experimental results with high electric field molecular dynamics simulations. This finding further shows that the observed atomic displacements in FIM are due to the field redistribution rather than due to real atomic movements. This first work has provided more insights into the physics of image formation in FIM. In addition, this result shows the importance of accounting for a realistic field distribution at the surface of the FIM specimen, which builds upon the simple model only based on geometrical considerations developed in the past [18,19]. In this paper, we propose to extend and improve this model to enable to understand image FIM formation in more realistic and general cases adapted to the formation of the image in the three-dimensional field ion microscope. A comparison of experimental and simulated images is provided on tungsten which is the standard material for FIM. The ultimate spatial resolution and detection efficiency are estimated based on the model and compared to experiments. A quantitative agreement is obtained showing the ability of this model to push the performances of the 3D FIM to its ultimate limits.

2. Methods

2.1 Experimental details of the 3DFIM and theoretical consideration

In a FIM experiment, the specimen of end radius *R* is biased to a potential *V* of several kilovolts. Due to lightning-rod effect, an intense electric field is produced at the apex. This electrostatic field is inversely proportional to the radius of curvature at the specimen's apex as shown by the Eq.(1).

$$F = \frac{V}{k_F R} \tag{1}$$

Where k_f is a geometric factor [20].

Under the effect of this intense electrostatic field, the gas atoms are polarized and then attracted towards the surface of the specimen. When an atom is close enough to the surface, it can be ionized and accelerated by the electric field towards the detector system. Image gas ionization is generally understood as a quantum process of electron tunnelling from the gas atom to the tip surface. Note that gas atom is assumed to be thermalized to the cryogenic sample temperature. This effect was experimentally evidenced by E.W. Müller in 1951 [21] and the theory was developed in the following years. Gomer provided approximate calculations of the tunneling probability [22,23]. Ionization is in

this model produced by electron tunneling across the energy barrier existing between the atom and the metal surface. The tunneling transmission is calculated using classical Jeffreys-Wentzel–Kramers–Brillouin (JWKB) method [24]. These expressions are generally in good agreement with experimental results. In the simplest approach, the tunnelling probability T(*I,F*) is modelled by

$$T(I,F) \sim exp\left(-6.83 \times 10^{9}\left(\frac{I^{3/2}}{F}\right)\right) \quad (2)$$

where I is the ionization energy in eV of gas atom in vacuum, and F the applied electric field in V/m.

The ionization probability is here calculated at its maximum, when the atom is located at the critical distance of ionization x_c. This distance is the shortest distance for which ionization of the free imaging gas atom above the surface can occur, and writes:

$$x_c = \frac{I - \phi}{eE} \quad (3)$$

Where $\phi$is the the Fermi level.

Each surface atom is seen as a protruding feature with a higher local curvature than the average curvature of the specimen, thereby enhancing the local electric field. These surface atoms are also locations where the gas atoms can adsorb and further enhance the roughness of the surface, and consequently the local field [25,26].

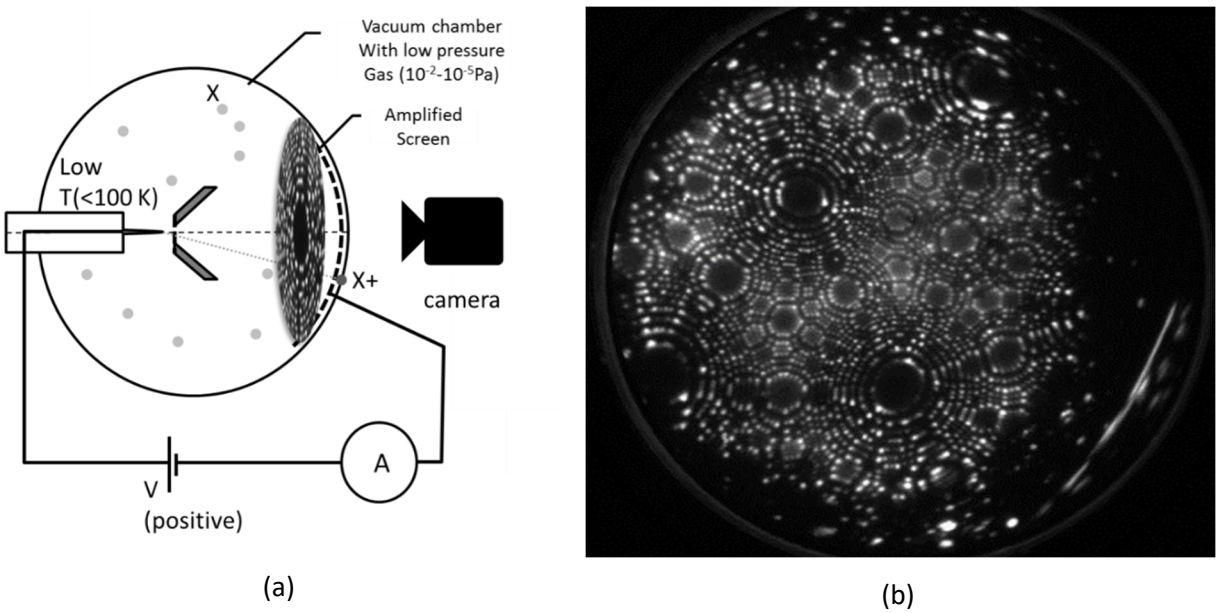

(a) (b)

Figure 1 *: Field ion microscopy experimental setup (a). Tip is placed in a vacuum chamber at low pressure gas (He, Ne,…) and cooled at a temperature below 100K. Experimental Field ion micrograph of a tungsten sample (b). Each bright spot on the screen corresponds to an atom on the surface of the tip apex.*

At x_c above the surface, each surface atom is then a local site for imaging gas ion emission. An ion beam (a few thousand per second) is emitted, and accelerated by the electrostatic field. The electric field lines are strongly diverging and a magnified image of the surface is produced on the imaging screen placed at 3–10 cm away from the specimen.

Note that eq. 2 is an approximation of the actual tunneling rate above the specimen's surface. For instance, it does not take into account the real three dimensional distribution of the electrostatic field above the atoms, **which is also diverging right above surface protrusions,** or the presence of a layer of adsorbed gas atoms on the surface that is experimentally of great influence [27]. The influence of the real electronic structure of alloys is also not taken into account. More refined theories are necessaries to fully address the contrast existing on the surface. For instance tunneling probabilities calculated using the Tersoff-Hamann approximation shows that the electronic structure greatly influences the tunneling rate [28]. Indeed, at the critical distance of ionization the tunneling rate is proportional to the surface local density of states, which may give additional enhancement of the contrast in the case of alloys. Here, we will neglect these enhancements, but eq. 2 could be modified to account for these effects.

The imaging system is composed of a microchannel plate, to amplify the signal, and a phosphor screen, to convert the electrons signal in photons signal. On the phosphor screen it is possible to observe a projection of the specimen's surface with a high magnification ($\sim 10^6$). As represented in the Fig.(1.b) each bright spot corresponds to the projection of an atom position at the surface of the tip. At low temperature, the size of spots is about 0.2 to 0.5 nm in diameter. The concentric rings results from the intersection of the crystallographic planes on the material and the hemispherical surface of the tip apex.

In 3D FIM experiments, it is necessary to image the surface and field evaporate the specimens at the same time. The applied DC voltage is controlled to get slow field evaporation of the material (from 10^{-2} to 10^5 atom/s in the general case). In specific cases, such as with tungsten, the evaporation field is too high and, when this field is reached, atomic resolution is lost because the gas atoms are ionized too far from the specimen's surface. **Experimentally, the quality of FIM images is optimized for a defined electric field above the surface named best image field (BIF). For He as an imaging gas, this field is about 45 V/nm. On another hand, field evaporation is controlled by materials properties (evaporation field constant), as it will detailed in section 2.3.1. For tungsten, field evaporation occurs at electric field close to 60 V/nm.** It is possible to solve this problem by using additional short nanosecond voltage pulses superimposed to the DC voltage [16]. The FIM contrast is then controlled by the DC voltage and the controlled field evaporation is triggered at or near to the top of voltage pulses. A regular evaporation rate is maintained during all the experimentation with a feedback control on the total (DC+pulsed) voltage. **The appropriate ratio of the amplitude of the high-voltage pulses to the DC voltage is material dependent (V_P/V_{DC} around 30-35% for tungsten).**

2.2 Image reconstruction

Here, an algorithm modified from that of Dagan et al. [16] was used to retrieve the position of the atoms on the screen, and thereafter perform a reconstruction in the analysed volume. These sequential 2D hit positions extracted from the FIM images form a space called "image space" that we

refer to as the “detector space”. Applying a reverse projection from the coordinates of these positions generates a reconstruction of atomic positions.

First, the raw images are optimized by image processing. The micrograph in Fig.(2a) was obtained on a tungsten wire oriented, along the <011> direction, and prepared by electrochemical-polishing with a solution of 5% NaoH in water with a voltage in the range of 5–8V. FIM was performed at 40K with a pulse fraction of 35%, and He as an imaging gas, under a pressure of 10^{-3}Pa. Several million of atoms were collected from the controlled field evaporation of the specimen. A region of interest is cropped and showed in Fig.(2b). Brightness and contrast are adjusted, a noise thresholding is applied using a representative intensity histogram of the set of equalized images. The best threshold is chosen as the minimum between the peak corresponding to the noise and the peak of the actual spot signals. A median filter is used to reduce the local noise level and images are smoothed with a mean and a Gaussian filter (σ~1 pixel). The final result, following image processing, is presented in Fig.(2c).

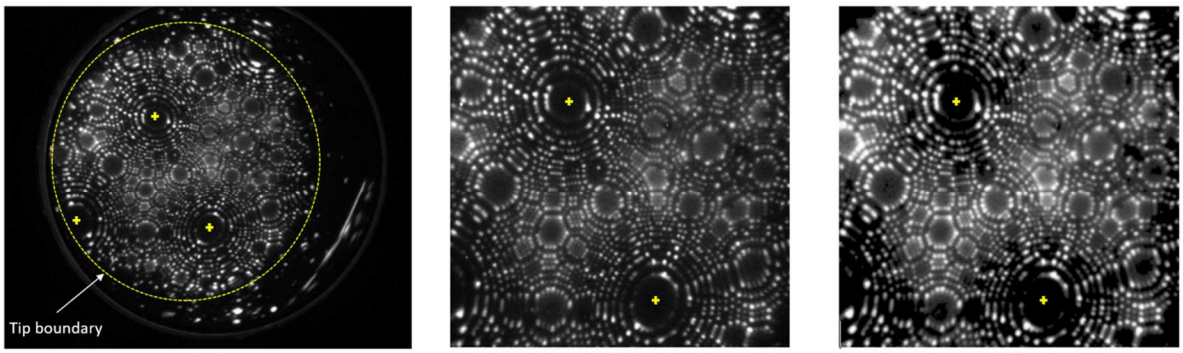

Figure 2 : *Raw image of tungsten record with CCD camera at 3.5 fps, (011) poles are identify by yellow crosses (a). Cropped image on a region of interest where the resolution is enough to apply the recognition algorithm (b). Final image after contrast improvement and noise reduction steps (c).*

Second, atom identification is performed by recognition of sudden changes in contrast between two successive images that correspond to where atoms were field evaporated (Fig.(3a,b)). Indeed, at a slow evaporation rate, the contrast between two successive images seldom varies, and the only source of significant variation is the removal of a limited number of atoms. When an atom is removed, the contrast locally changes from bright to dark at this precise location. The direct subtraction of image intensity map between two successive images reveals that field evaporation occurred at specific positions. The resulting differential image in Fig.(3c) presents bright contrasts at the location where atoms were field evaporated.

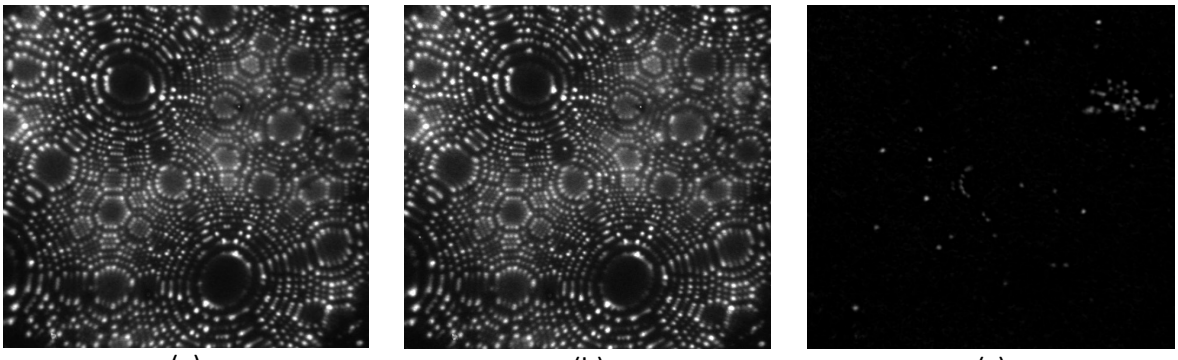

Figure 3 : *Results of the difference after thresholding (c) between an image take at time t_1 (a) and*

an image took at time $t_1 = t_0 + \Delta t$ (b). Each bright spot represents an evaporated atom during this interval of time Δt.

Then, the detection of local maxima on this resulting image is done in three steps. The first step uses an ordering (or sorting) filter that sorts pixels by grey level value in a given neighborhood around the considered pixel, i.e. similar to a median filter. More details can be found in ref. [29]. In this case we use an order filter of the 'maximum' type using a mask as showed in Fig.(4a). Pixels of the original image, showed in Fig.(4b), are scanned one after the other. For each of them, the algorithm looks in the neighboring pixels, contained in the mask having a value of 1, for the pixel of the image which has the highest grey level. Then this value replaces this value of the analyzed pixel on the original picture. The results of this filter using the mask of Fig.(4a) applied on pixel of Fig.(4b) is illustrated in Fig.(4c). Note that the example illustrated by Fig.(4) is an idealised case.

The second step in the process is to compare, with a logical test, the original image pixels values and the new pixel values of the filtered image. For a given pixel, the grey level on the filtered image is below the grey level on the original image if this pixel corresponds to a local maximum. Pixels that correspond to this criterion are then marked, assigning them the value 1. All other pixels that do not respond to this criterion are marked with the value 0. The image finally obtained, illustrated by Fig. (4d), corresponds to the local maxima. For optimal detection, the size of the mask must be adapted to the size of the spots (typically the first odd value below the average size of the spots on the images). The magnification evolves throughout the experiment, but the size of the mask remains suitable over a range of a few kilovolts. The size of the spots will tend to decrease as the radius of curvature of the sample increases. On a range of a few kilovolts evolution, the decrease in diameter of the spots on images will only be one or two pixel(s). The mask will remain efficient for spot detection with this small change in spot size.

After these two steps, on field ion micrographs, each detected local maximum on field ion micrographs is composed of a group of several connected pixels. The final step is a clustering approach, where a label is given to each group of pixels and a centre-of-mass is calculated to define precisely the position of each atom.

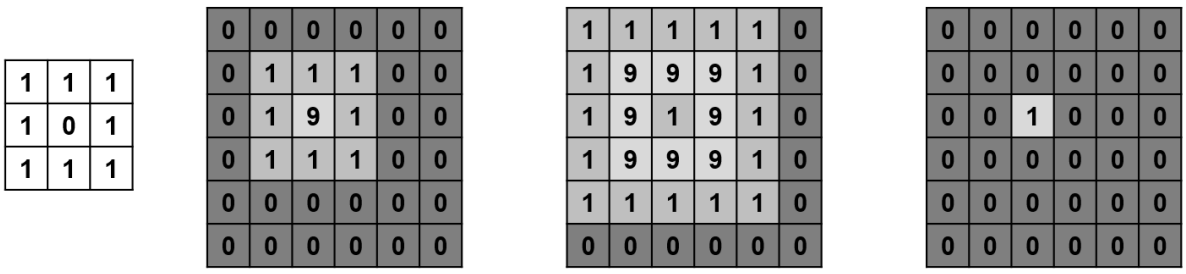

Figure 4 *: Main steps of the atom identification filter on an example of few pixels. Typical 3x3 pixels mask used to filtered images (a), pixels with value 0 in the mask are taken into account during the search for the maximum grey level. Image with a local maximum (b), value represents the grey of pixels. Filtered image result (c) after applying the order filter type maximum with 3x3 pixels mask. Final binary image obtained after a logical comparison between original images a filtered image (d),*

local maximum is located with value 1.

After image processing, a count of the bright spots can give an estimated number of field evaporated atoms between two successive images, and an estimate of the evaporation rate. From this number, it is then possible to calculate the corresponding volume and so determine a depth increment between two successive images using conventional reconstruction procedures used in atom probe tomography [30]. After this second step, a 3DFIM analysis consists in a list of impact position on the image screen that formed a space called 'image space' (Fig. 5).

Note that all these reconstructions algorithms were developed in C# and included in a home-made data processing software. For each step, a processing module was created in the software (basic image processing, atom detection, ...). The calculation time is obviously dependent on the performance of the machine used. On a standard desktop computer (Intel core i5), for a sequence of 10,000 images of 1000 x 1000 pixels the detection of spots by the method of local maxima takes a few tens of minutes. The calculation of differential images on the same sequence of images takes, at most, a few tens of seconds. Finally, atom detection is the longest step in the reconstruction process and takes in average a few tens of minutes. The following calculation steps only add a few extra seconds to complete the reconstruction.

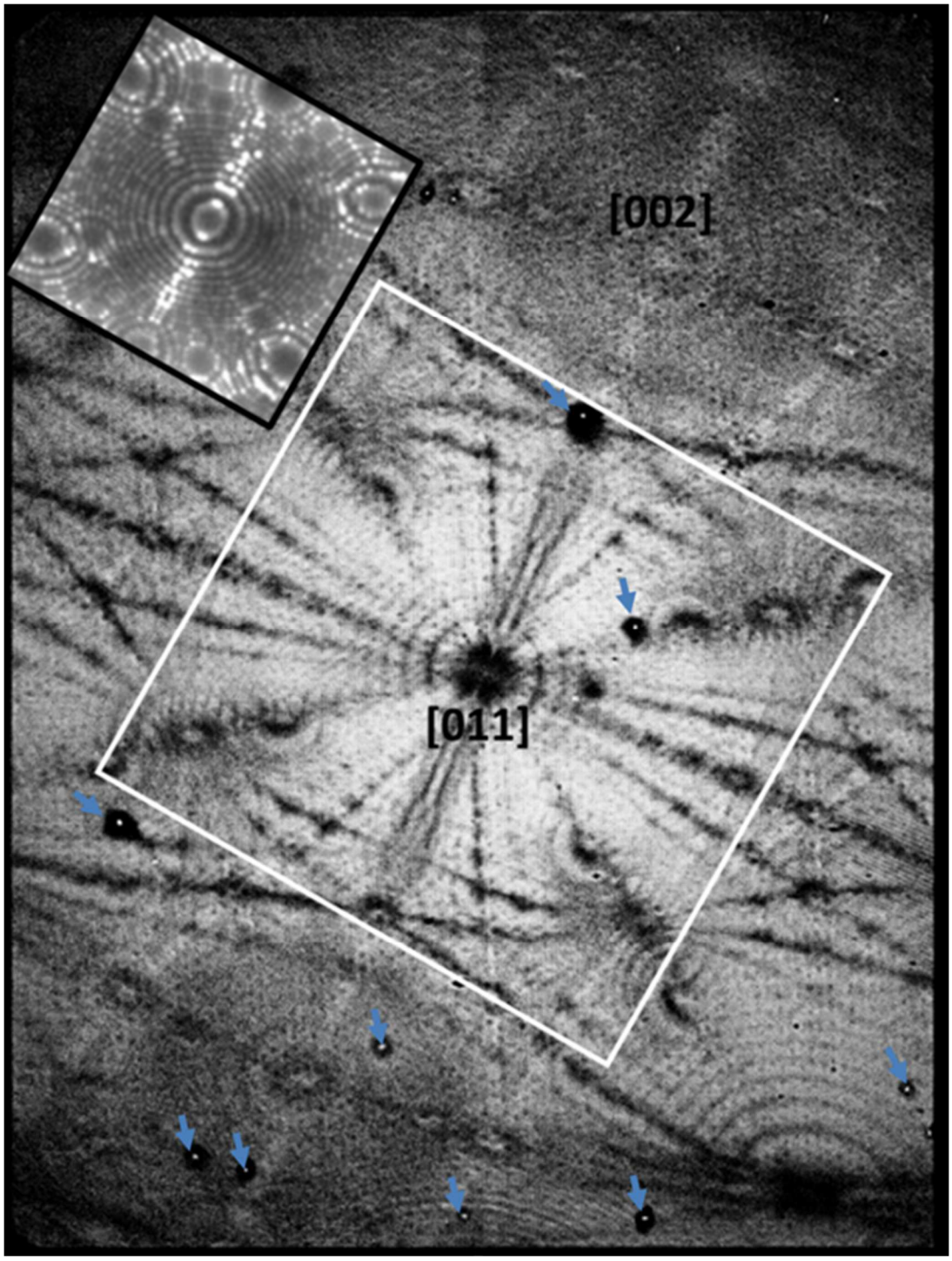

Figure 5 : Stacking of the atoms positions on the detector (Detector hit map). Artefacts like concentric rings, dark and bright lines, induced by the crystallography-related faceting of the specimen, are clearly visible. Note that small dark spots (mark with arrows) are due to imperfection on the phosphor screen. The inset shows the corresponding FIM image in the delimited white box

The transformation from the 'image space' into the specimen space consists in applying a reverse projection algorithm. The projection law of the FIM is considered identical to the projection used in

atom probe tomography. From the (X,Y) positions of impacts, (x,y,z) positions of atoms are reconstructed using the extended Bas protocol described elsewhere[1–3,30].

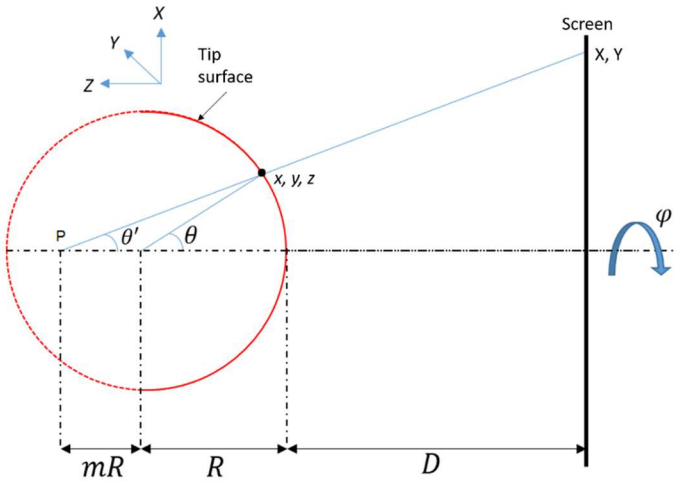

Figure 6 : Schematic of the quasi-stereographic projection from a projection point located at a distance R (m + 1) from the surface of the hemisphere on a plane. A position (x,y,z) at the tip surface is projected to screen assuming classical a quasi-stereographic projection (point projection P situated at a distance mR from the tip center).

The position on the surface of the tip of an atom detected at positions X, Y on the screen can be calculated from the quasi-stereographic projection law (Fig. 6). First, we can express the angles θ' and φ', which are the projection angles of ions to the detector, derived from the impact position (X,Y) following:

$$\begin{cases} \theta' = \arctan\left(\dfrac{\sqrt{X^2+Y^2}}{D}\right) \\ \varphi' = \arctan\left(\dfrac{Y}{X}\right) \end{cases}$$

Then from these two angles we can express θ and φ :

$$\begin{cases} \theta = \theta' + \arcsin(m\sin(\theta')) \\ \varphi = \varphi' \end{cases}$$

m defines here the distance between the hemispherical apex center O, and the projection center P (OP=mR). A change of coordinate system allows these coordinates to be expressed in the Cartesian coordinate system whose origin is located at a distance D from the detector. These coordinates will hereinafter be called back-projected coordinates:

$$\begin{cases} x = R_i \sin(\theta)\cos(\varphi) \\ y = R_i \sin(\theta)\sin(\varphi) \\ z = R_i(1-\cos(\theta)) + Z_i \end{cases}$$

R_i is the radius of curvature at apex of the tip corresponding to image number i. Z_i is the eroded depth from the tip to image i and is calculated as the sum of the increments in depth $(d_{z,i})$ between each image from 0 to i. This value must be added to the z coordinate to account for the sample

erosion. The depth increment ($d_{z,i}$) between each image can be determined by counting the number of images necessary to completely evaporate the surface plane of a given family as explained in the work of Dagan et al. [16]. Another approach consists in using the Extended Bas protocol [30–32] to estimate an evaporated volume between two successive images. This method requires knowing the number of atoms evaporated between these two images. Thusly, an estimation of the detection efficiency is injected as a parameter to reconstruct 3D datasets.

Note that the tip of the specimen is assumed to adopt a hemispherical shape of radius R_i. The evolution of the radius of curvature is determined assuming a constant shank angle evolution during field evaporation, or by using voltage V evolution to deduce R through Eq.(1) assuming constant field evaporation strength. We may note that this method is far from being perfect since FIM collects a larger field of view compare to APT. As a result, the image is not free from distortions introduced by the limited hypotheses of the reconstruction algorithm. However, in this paper we will focus on spatial precision, or spatial resolution degradations which are not affected by these global deformations [1,33,34].

Fig.(7) shows a series of subset of the reconstructed volume from the dataset introduced in Fig.(5). The complete volume was $55 \times 55 \times 65\, nm^3$ containing around five million atoms. Each subset shows specific families of atomic planes and, along specific directions, atomic columns. The reconstruction was performed using a constant field factor, an initial radius of curvature R_0 estimated from FIM images, the average atomic volume of tungsten atom of $1.57 \times 10^{-2} nm^3$, and an average detection efficiency of 80%. After adjusting the reconstruction parameters (field factor, image projection factor), the average interplanar distance between (011) atomic planes in the depth direction is $d_{011} = 2.24 \pm 0.05$ Å (close to the theoretical distance of tungsten 2.23 Å). Post reconstruction deformations exists but are small considering the simplicity the reconstruction algorithm. For instance, angle between the two 011 direction represented on the Fig.(7) is $84.5°$, whereas it should theoretically be 90°. Distortions caused by issues inherent to the reconstruction have been discussed in several paper[31,35].

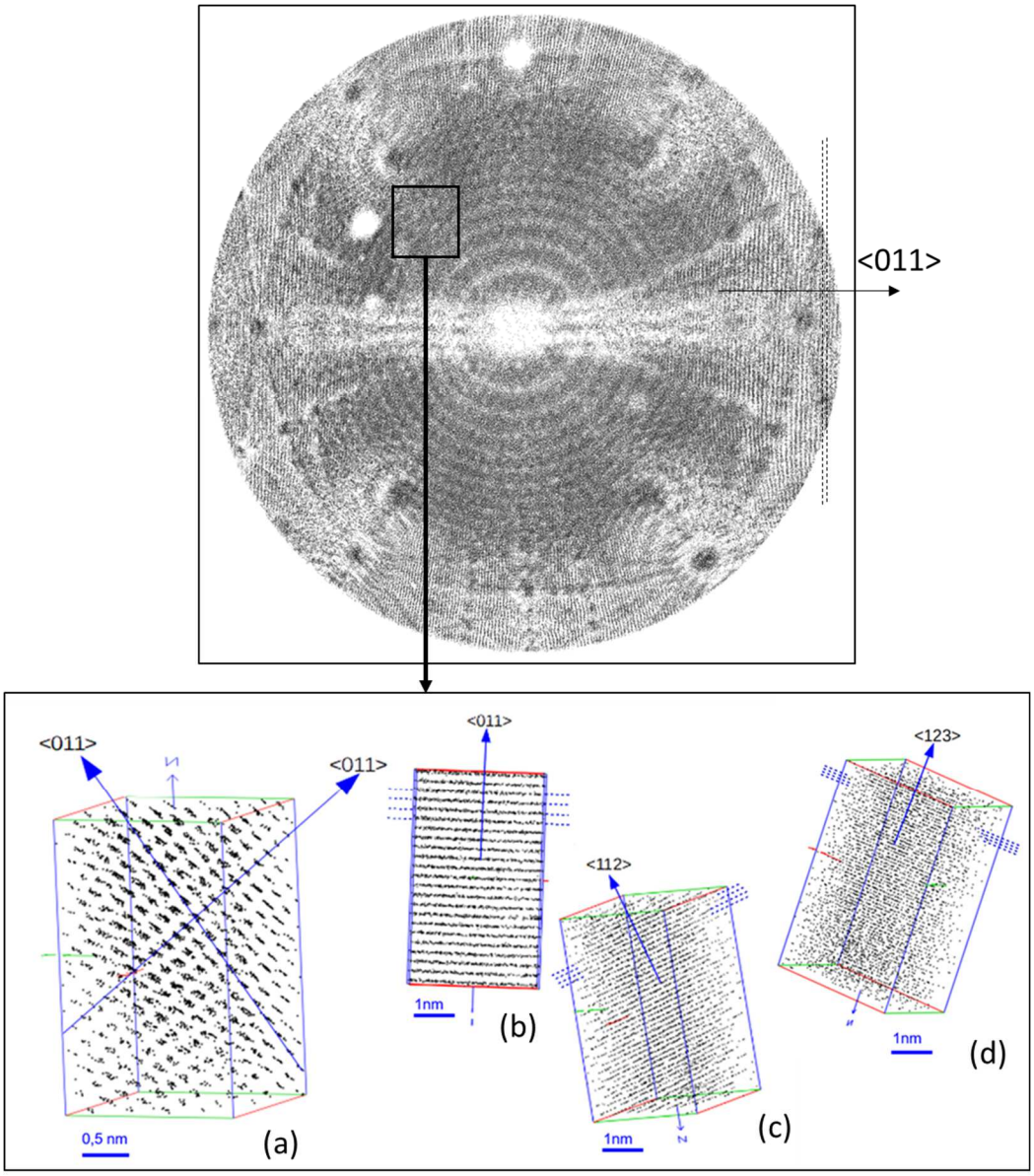

Figure 7 *: Small volume of* $3 \times 3 \times 5\ nm^3$ *selected in the complete reconstructed volume (top image) in different orientations. Several families of planes (b)(c)(d) and atoms column (a) are visible in some specific orientations of this volume. (011) planes are also reconstructed laterally on some regions of the whole reconstructed volume (e).*

2.3 FIM modelling

Modelling FIM images requires three steps. First, the atom-by-atom sequence of field evaporation from a virtual specimen must be calculated. This step is performed using the Robin-Rolland algorithm [36] developed for the interpretation of atom probe tomography imaging processes. Second, the tunneling probability of the image gas is calculated at different stages of the tip's field evaporation. Last, the projection of ions from the specimen's surface onto a plane simulating the projection on the screen or detector is evaluated. This last step requires an accurate calculation of the electric field distribution in the open space between the specimen and that plane.

2.3.1 Robin-Rolland field evaporation Model

The Robin-Rolland algorithm enables the dynamic calculation of the electric charge distribution at the surface of a virtual FIM specimen, assuming the charge being localised at the positions of surface atoms. In the present approach, the simulation space is only defined by the three-dimensional coordinates of each atom of the emitter and no additional support points (i.e. grid) are introduced, neither inside the virtual specimen nor in the surrounding space. Classical electrostatic theory describes the perfect conductor object to a given voltage in vacuum as an equipotential surface enclosing a zero-field volume. This equilibrium is instantaneously reached through the redistribution of the free electrons from within the conductor. As a result, the volume charge density is strictly zero, while there is a non-zero surface charge density $\sigma(\vec{r})$, distributed all over the surface S of the virtual specimen.

The above calculations of the charge distribution are based on the assumption of a smooth surface of a conductive material considered as a continuous medium. As a result, the charged surface is considered as an infinitely thin layer, and classical electrostatics can be applied. In a real material, the charge is found to concentrate on the atoms at the surface. These surface atoms may be considered as partial ions [37–40], with the most protruding atoms building the strongest charge, and therefore being the locations of the highest external field.

The elementary surface occupied by each atom is considered as a constant S_{at}. By applying a constant electrostatic potential, only the atoms (i=1,N) of the surface will be subject to a non-zero surface charge density σ_i. The charge q_i is given by the product $\mathrm{S_{at}} \times \sigma_i$. To calculate this surface charge, the discretized form of the Robin equation is used:

$$\frac{q_i}{S_{at}} = \frac{1}{2\pi} \sum\nolimits_{k=1,k\neq i}^{N} q_k \frac{\vec{n}_i . \vec{r}_{ik}}{\|\vec{r}_{ik}\|^3} \tag{5}$$

Here $\overrightarrow{n_i}$ denotes the outward normal to the surface at the position of the atom *i*, and $\overrightarrow{r_{ik}} = \vec{r_i} - \overrightarrow{r_k}$.

For the purpose of finding the charge distribution over the field emitter's surface, one can now construct a sequence $q_{i,n}$ for each atom *i* . $\frac{q_{i,n+1}}{S_{at}} = \frac{1}{2\pi}\sum_{k=1,k\neq i}^{N} q_{k,n} \frac{\vec{n}_i . \vec{r}_{ik}}{\|\vec{r}_{ik}\|^3}$This sequence tends toward the charge distribution at equilibrium, at least for a convex surface. In the convergence process, the atomic surface is chosen to ensure that the total charge of the system remains constant. Once the convergence is reached, the charges are rescaled to give the correct applied voltage V_{DC} using the

application of the **Coulomb law to the distribution of charge (charge and potential being linked by** $\boldsymbol{V(\vec{r}) = \frac{1}{4\pi\epsilon_0}\int \frac{\rho}{r} dV}$)

This last equation represents a system of N coupled, linear equations which can be solved numerically. The brute force resolution of this system of equations exhibits a $\mathcal{O}(N^2)$ complexity, N being the number of surface atoms. To avoid such a computational effort, equation (6) was optimized using a Barnes-Hut algorithm [41] approximating the long range interactions. In this approach an octree structure with the position of the N surface atoms was described reducing the complexity to ~ $\mathcal{O}$(NlogN). More details about the procedure is described in details in [36].

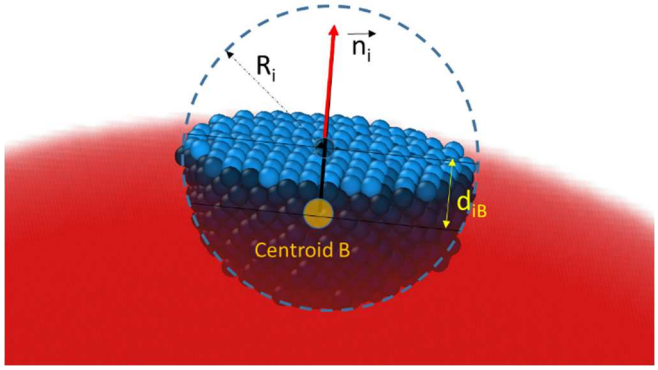

Figure 8 *: Method used to estimate the surface normal to the tip composed of atoms. The centroid B of atoms situated in a small sphere of radius* R_i *centred on atom* A_i *is calculated. Surface normal vector* $\vec{n}_i$ *is the unit vector of direction* $\overrightarrow{BA_i}$**.** $\| \overrightarrow{BA_i} \| = d_{iB}$ *enables to discriminate surface and bulk atoms.*

We modified slightly the model to describe any arrangement of atoms inside the specimen's tip. Identification of surface atoms from arbitrary structures, as well as definitions of normal directions for these N surface atoms are required in Eq.(5). Surface atoms are atoms surrounded by an asymmetric distribution of neighbors. To quantify this asymmetry, a simple method derived from work of Boll et al. was developed [42]. A sphere of radius R_i is placed on all atoms of the simulated volume (Fig.(8)). The position B of the centroid calculated on all atoms inside the sphere, enables the calculation of the vector $\vec{u}_{Bi}$. Atoms for which d_{iB} the length of $\vec{u}_{Bi}$, is higher than a user-defined criterion δ_B are defined as surface atoms. The direction of $\vec{u}_{Bi}$ gives directly the normal direction to the surface. The choice of R_i will be a compromise between a smooth definition of the normal direction and the computation time. Indeed, the higher is R_i, the larger is the number of atoms inside the sphere, and the more accurate is the estimation of the local normal. R_i is chosen to maintain approx. 50–100 atoms inside the sphere. The user criterion δ_B is an ad-hoc parameter chosen to keep a monolayer of atoms at the tip surface. In this case, δ_B is fixed to 0.2 nm.

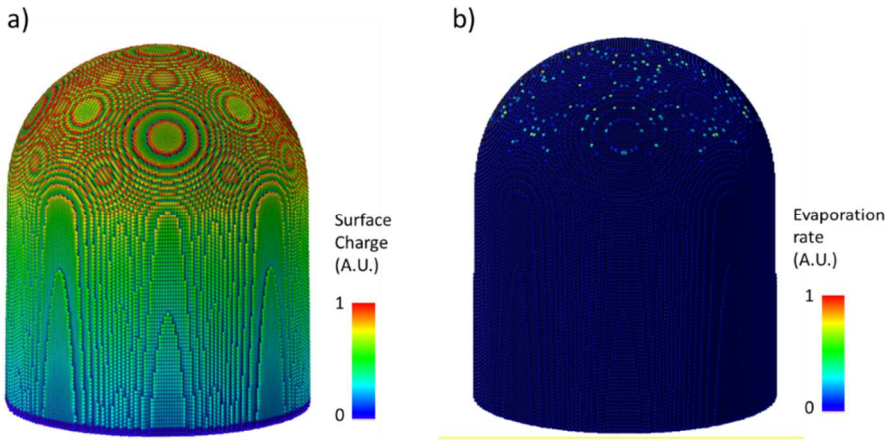

Figure 9 *: Surface charge (a) on atom represented by a color scale. (b) Evaporation probability or rate calculated from eq. 9.*

Once the surface atoms are determined, an optimized version of Eq.(5) is iterated. The rapid convergence of the RRM, starting from a uniform value of charge, enables the calculation of the charge distribution across the virtual specimen's surface in a few iterations (convergence criteria $<10^{-10}$ in less than 100 iterations, Fig. 9a). We may note that error decreases exponentially with iterations. The external field is directly derived from the charge distribution at any place using Coulomb's equation. Once again, the octree structure is used to solve this equation, ensuring an acceptable computation time. The electric field just above the surface is calculated directly from the surface charge provided by the model.

The field evaporation order is evaluated using the strength of the electric field (or charge since it is proportional) over all surface atoms, and using the evaporation field of each atom. We applied the procedure proposed by Vurpillot et al. [43]. The rate of field evaporation K(s^{-1}) of a given surface atom A_i is known to follow classical Boltzmann's equation

$$K_i(s^{-1}) \sim \nu_0 exp\left(-\frac{Q(F_i)}{k_B T}\right) \tag{6}$$

F_i being the surface electric field applied to the atom, and $Q(F_i)$ a field dependent energy barrier. In the simplest approach, on each atom A_i, it can be defined a unique expression for $Q(F_i)$ that follows a monotonous relationship with F_i [2].

$$Q(F_i) \sim C_{Ai} \times \left(1 - \frac{F_i}{F_{Ai}}\right) \tag{7}$$

Assuming C_{Ai} ~1 eV an energetic parameter proportional to the sublimation energy for most of the elements, the evaporation rate is strongly dependent of the ratio $\frac{F_i}{F_{Ai}}$. F_{Ai} is a parameter that depends on the elemental nature of elements, and of the bonding interaction energies with neighbors. The rate of evaporation K_i can be calculated for all surface atoms, and the choice of the

atom to be field evaporated can be taken using this table of rate. A Monte Carlo algorithm can be useful, as used in ref. [44–46], but at T<80 K, C_{Ai}/k_BT~150, which means that the probability to be field evaporated is sufficiently high only for the few atoms with the highest ratio $\frac{F_i}{F_{Ai}}$ (Fig.(9b)). The low temperature used in FIM makes the field evaporation process strongly field dependent and quasi deterministic.

An estimate of $F_{Ai}$is required in this algorithm. We generally assume a constant value for each element, that is calculated on the basis of the fields estimated for the pure elements[1]. Some approaches have been proposed to give an accurate expression that depends of the local environment of each atoms to calculate a local critical electric field to induce field evaporation [47–49]. Note that this is expected to be integrated in future implementation of the model. When an atom is selected for field evaporation, it is simply removed from the surface, and a new list of surface atoms is generated. The surface charge of the evaporated, ionized atoms gets back to the total charge of the virtual specimen, and the distribution of surface charges is recalculated. The convergence of the algorithm is then extremely fast, since the charge of most of the atoms are only slightly modified by the removal of a single partial charge, i.e. 5-10 iterations are generally sufficient to re-calculate the charge distribution at the tip surface.

2.3.2 Electron tunneling and ionization rate

Once surface electric field *F* is known, it is straightforward to evaluate the electron tunnelling rate above each surface atom and then to determine the ionization rate. The critical distance of ionization and the tunnelling rate are calculated for all surface atoms through eq. (3) and (4). Obviously, we neglect tunneling that can occur farther from the surface, due to the rapid decrease of the field with the distance to the tip. Eq. 2 provides an approximation of the tunneling rate. If we consider the first ionization energy of He (I=24.5 eV), within a field range ±30% of the best image field (BIF=44 V/nm), eq.2 can be simplified to $T(f = F/BIF) \sim exp\left(-\frac{A}{f}\right)$, with A~18.3 (assuming more refined models, A is a field varying parameter, but variation with field is extremely reduced in the field range).

In practice this semi-constant A can also be adjusted to provide better visual agreement with experiment (in the range 10–20, in this paper A was adjusted to 12) since the theoretical transparency also neglects a lot of second order parameters (gas adsorption layer, local density of state, etc…) .

2.2.3 Projected image in FIM, 3D FIM and APT

Atoms from the imaging gas are generally thermalized to the specimen's base temperature. As a result, we may consider that the initial velocity of the produced ion is almost zero ($E_c \sim k_BT$~2-10 meV in FIM). The position situated at the critical distance of ionization x_c, along the normal to the surface is chosen as the departure position of the center of the ion beam generated by field ionization. From this place, the trajectory of the ion is computed. The ion trajectory toward the detector is computed from the Newton motion equation as originally proposed by Vurpillot et al. [50], using a Runge-Kutta numerical scheme. Although the calculation method makes it possible to compute the trajectory

over any distance, we chose to calculate the trajectory up to 1 micron, and then use conventional extrapolation at large distance up to a virtual planar detector.

Between the field evaporation of 2 atoms, the still surface of the virtual specimen is imaged onto the FIM screen. Each surface atom is the center of a beam of image gas ions that is projected by the electric field onto the screen. We can produce a map of this projection by plotting the FIM atom position map (or FIM hit map, Fig. 10a). Using these positions, a virtual FIM image is generated. Each atom location on the screen is used as a seed for a Gaussian distribution to mimic the distribution of ion intensity on the screen produced by a single atom at the tip surface. A FIM image is produced by the superimposition of thousands of light spots on the screen produced by the local ionization above surface atoms of the sample. Knowing the position of each ion beam on the detector, the tunneling rate must be evaluated for every ionization site. Assuming intensity being proportional to the tunneling rate, it is therefore trivial to generate a simulated FIM image. On the screen, we assume that each atomic position produces a lateral distribution of intensity that follows a Gaussian shape. The standard deviation of this Gaussian is fitted to the experimental resolution of FIM image that depends on the specimen's temperature and image gas and varies between 0.2 to 0.5 nm [6]. The peak of the Gaussian function is adjusted to the relative tunneling rate above each atoms. By evaporating the virtual specimen atom-by-atom, and computing the ion trajectories of every field evaporated atom (Fig. 10b), a cumulative hitmap similar to those obtained by APT, as well as a 3D reconstruction of the evaporated volume can be calculated. At the same time, it is possible to store the FIM atom position of each field evaporated atom just before removing it from the surface (Fig. 10b). This position defines the ideal 3DFIM atom position. By cumulating these positions for millions of atoms, an ideal 3DFIM hitmap (free from any detection algorithm artefacts) can be generated.

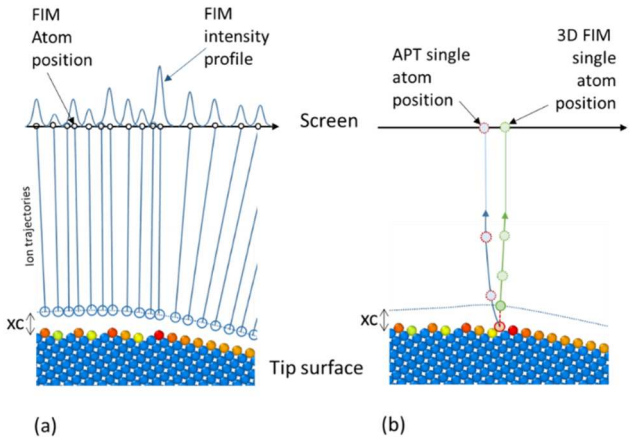

Figure 10 *(a) Schematic drawing of the calculation of FIM spot positions and FIM intensity map (a) and the calculation of the single position in APT and 3D FIM (b). In (a) the image is formed between evaporation of 2 atoms over the whole surface of the tip. Each surface atom location is projected to a*

ideal FIM hitmap. These positions are used to compute a virtual FIM image, using an intensity distribution for each FIM atom position.

An example of the FIM hitmap produced by the computation of ion trajectories from the critical distance above each of the surface atoms is presented in Fig.(11a). The virtual sample is a face centered cubic structure tip, with an embedded precipitate having a diamond structure and a relative evaporation field 20% higher than the matrix. The radius of the virtual specimen is 25 nm. Using these positions, and the electrostatic field distribution above the surface, a FIM image is generated (Fig. 11b). FIM hitmap (Fig 11a) and FIM image (Fig11 b) can be generated after the virtual field evaporation of thousands of atoms from the specimen. These images can be compared to the APT image produced by field evaporating a thin layer of atoms, i.e. the equivalent of a hitmap collected in APT (Fig.11c). Because the field ionization occurs farther from the tip's surface compared to the field evaporation, the image gas ions and ions originating from field evaporation of the surface atoms do not follow the same trajectories. The typical artefacts that affect the spatial resolution in APT are hence visually less pronounced in FIM. These artefacts were quantified in a previous article [44].

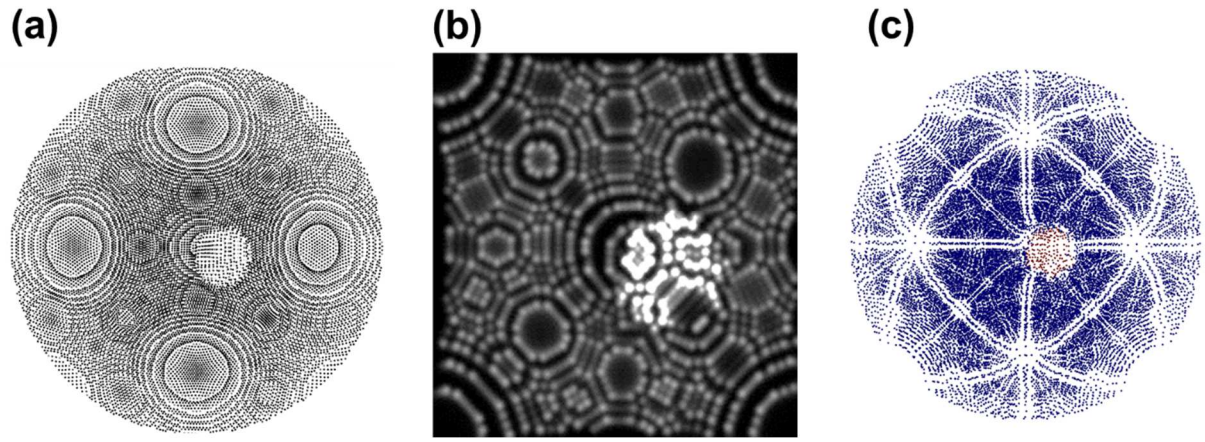

Figure 11 *(a) Ion hitmap of the positions of surface atoms in the case of a FCC cristal with a spherical diamond structure inclusion (field evaporation 20% higher than the matrix atoms) close to the tip centre, assuming a critical distance of field ionization given eq. (3) (no difference in electron work function between phases were assumed) (b) simulated FIM image, assuming the tunnelling probability and the critical distance of ionization. Difference in contrast between phases is uniquely linked to the calculated surface field (c) simulated APT hitmap for the evaporation of 3 atomic monolayers on the detectors. Trajectory aberrations of field evaporated atoms are strongly influenced by the charge distribution around evaporated atoms in the first steps of flight (generating zone lines contrast)*

3. Application to a pure metal case (tungsten)

3.1 3D FIM simulation calculated on a [011] oriented tungsten tip

To assess the performances of the modelling tool in the prediction of image distortions in experimental FIM images, a BCC-tungsten virtual specimen was defined, with a diameter of 26 nm, aligned along the <011> crystallographic direction. 500000 atoms were virtually field evaporated to produce a virtual atom probe dataset (APT reconstruction and hitmap), an ideal 3DFIM hitmap, and every 50 field evaporated atoms, virtual FIM images were generated (10000 images were calculated). Note that to reduce the computation time, a region of interest was selected on the detector, equivalent to a field-of-view of approximatively 50° on the specimen. Results of these computations are presented in Fig.(12). The whole computation time was about 2 days on a 12-cores workstation (Intel Xeon 2.9GHz).

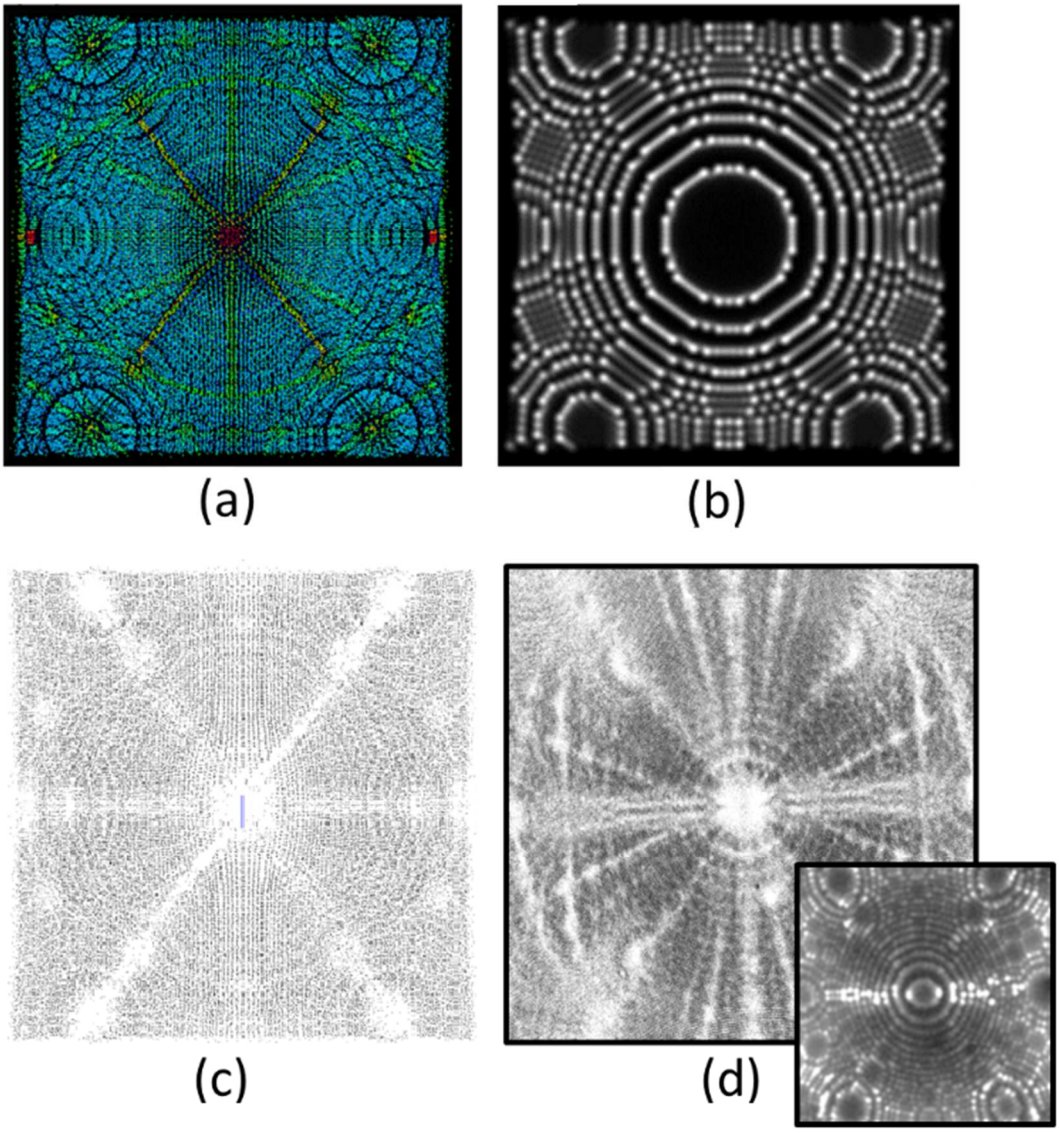

Figure 12 *FIM simulation of a tungsten tip, 26 nm in radius at the apex. 500000 atoms were field evaporated one by one following the proposed model (a) ideal 3DFIM hitmap on the screen, collecting 50° of field of view from ions projected from the initial position above surface atoms just before field evaporation. Ion starting position is at x_c from the surface, along the surface normal vector. Colormap indicated field strength at the moment of the field evaporation (Red=high field, Blue=low field). Note the presence of impact density variation induced by the dynamic local field distribution at x_c. (b) simulated FIM image at a given step of the tip field evaporation, assuming the tunnelling probability and the critical distance of ionization. (c) Hitmap produced by the detection of the initials positions of atoms obtained from the algorithm presented in section 2.2. The algorithm was applied to the sequence of simulated FIM images. Note the presence of additional depleted area on major zone lines and pole centres (d) comparison to the detection of atoms in a sequence of 10000 images produced following the evaporation of several millions of atoms on a [011] oriented tungsten tip (inset : Corresponding FIM image). Artefacts are strongly similar to the modelling approach.*

As observed in Fig.(12a), a single snapshot of ion impact (produced by ionization of ions above surface atoms) is rather homogeneous (Fig.(11a)). However, the accumulation of impacts generates significant distortions. Concentric density contrasts around the main low index poles are readily visible. Note that a perfect image should be almost homogeneous considering that only about ten (011) atomic planes were field evaporated and superimposed on the virtual detector. This kind of contrast is similar to the ring contrasts observed in field desorption images as discussed by Waugh et al. in ref. [51]. They suggested that this ring contrast was the results of a periodic variation in the magnitude of “aiming errors”, or of deflections of the metal ions, as the evaporating planes reach particular diameters. The rings are always of approximately the same size as the rings in the field-ion image, and obey the same law as the size of the rings observed by FIM, i.e. the diameter of the n^{th} ring from the centre varies as $n^{1/2}$. When the last terrace at the centre of a pole is smaller than a critical size, the plane will evaporate abruptly, giving rise to a flat surface of significant size. The alteration in the magnitude of the local field at a plane edge is accompanied by a small change in the direction of the local field [17]. This feature, is smoothed at the critical distance of ionization but it still gives rise to an average variation of the magnification at defined and regular places around the pole centre. A clear visualisation of this process can be observed in both simulation and experiment when looking at the 3DFIM contrast in the direction of the analysis. This is done by inserting an orthogonal slice in the 3D volume obtained by stacking-up a sequence of field evaporated images [52]. In Fig.(13a), an orthoslice was placed close to the pole centre in the simulated field evaporation image. Two (011) atomic planes were field evaporated during the sequence. The same procedure was applied to an experimental dataset (Fig.(13b)). In these figures, a bright filament along the depth axis is produced by the terrace field evaporation. The last atoms of the terrace at the pole centre evaporate steadily, and it is observed in both simulation and experiment a slight shrinkage of the

concentric ring around the pole. This shrinkage affects several successive terraces. This feature appears regularly giving rise to a periodic contraction of the magnification around the pole.

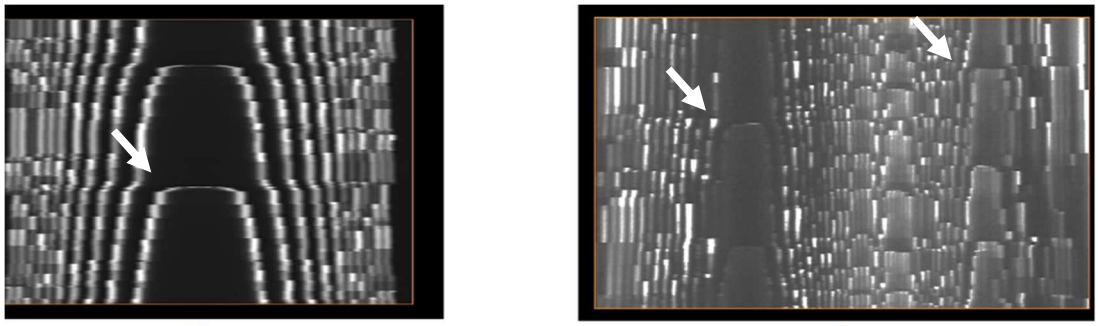

Figure 13 *Simulated (a) and experimental (b) FIM contrasts in slices parallel to the evaporation direction centred on the (011) pole. Two (011) atomic planes were fully evaporated. Shrinkage effects on terraces are visible on both simulated and experimental images (white arrows)*

In addition to these contrasts, zone lines and pole centres show variations in the density of impacts. When the last atoms from these regions are field evaporated, there are locally only few atoms on the respective atomic rows or planes. The local roughness varies strongly when a single atom is removed, giving rise to small deviations of the electric field lines as it was demonstrated in a previous study [17]. The sequence of field evaporation is however regular and periodic, so that the average deviation remains systematic, which changes the local magnification at these particular positions. Note that the impact of these deviations is almost invisible on still FIM images. Only an image-by-image analysis of FIM can highlight this phenomenon which is why it has seldom been studied up to now.

The calculation of a sequence of FIM images at increasing depths enables to evaluate the performances of our single-atom detection algorithm (section 2.3). Fig.(12c) presents the result of this computation applied to 10000 simulated FIM images produced every 50 evaporated atoms. Recalculated impacts positions are very close to the expected ones (Fig.(12a)). We may note that some additional depletions are produced at the centre of low index poles, and along major zone axes. Contrasts observed by simulation are very similar in intensity and location to contrasts experimentally produced (Fig.(12d)).

3.2 “Algorithmic” detection efficiency comparison

Since the model provides *a priori* knowledge of the initial volume, we can measure the efficiency of the detection algorithm introduced above. This detection efficiency will be named the “algorithmic detection efficiency”, since the produced simulation images are free from experimental additional

noise and biases (CCD dead pixels, MCP noise, MCP gain inhomogeneities, etc…). It will give us an optimal value of the expected detection efficiency in experimental cases. Fig.(14a) shows an ideal 3DFIM hitmap produced by the model. Fig 14b shows the same hitmap but calculated using the 3DFIM detection algorithm, using the sequence of 10000 produced FIM images during field evaporation. Fig14a is the image that should be obtained through a perfect detection of ion impacts. A slight degradation of the spatial resolution is observed, which is estimated to be in the range of half a pixel in the FIM images. The main visual artefact is the presence of depleted zones along the zones axes and the poles. To estimate the detection efficiency of the algorithm, in each pixel of the two maps, the number of hits was calculated, and the ratio of both numbers is calculated and shown in Fig.(14c). The algorithmic detection efficiency approaches 100% across most of the image. Along the zone lines and at pole centres, the performances of the algorithm are degraded. More advanced processing of the images may improve this efficiency, since most of the loss relates to the incapacity of the algorithm to separate some correlated field evaporated events giving rise to simultaneous impacts. The model is here an essential tool to optimize our detection algorithm and to estimate the best analysing conditions in 3DFIM (evaporation rate, detector spatial CCD resolution, etc…).

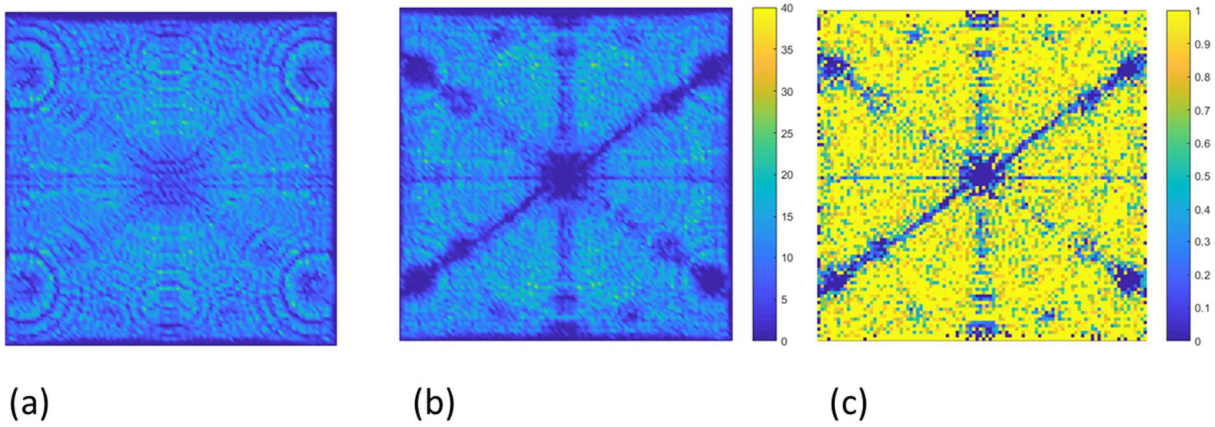

Figure 14 *: Comparison of the local density of impacts from the ideal 3DFIM hitmap (a) and from 3DFIM detection algorithm (b) (colorscale indicates the number of hits per pixel) (c) map of the detection efficiency of the algorithm calculated by dividing both images (yellow indicates 100% efficiency regions, dark blue 0% detection efficiency regions)*

3.3 Spatial resolution performances

The model developed in this paper can be used to estimate the spatial resolution loss introduced by the whole sequence of field evaporation, image formation, and algorithm detection. It was shown in section 2 that the experimental resolution could be in the range of a fraction of an angstrom in

depth. The lateral resolution of the 3DFIM, is in some places sufficient to laterally separate individual atoms on a low index atomic plane. (011) Atomic planes are observed laterally both experimentally and by simulation, indicating a lateral resolution better than 0.2 nm (Fig 7). This resolution is better than the intrinsic resolution of FIM, limited by the size of atoms on the FIM screen. This performance is possible because two lateral adjacent atoms are never exactly at the same depth within the specimen. In order to map more accurately the spatial resolution performances, and to estimate the impact of the field imaging process on the spatial resolution the Fourier based method described in [1,53] was used on the simulated and experimental reconstructions. Using this method, a 3D map of the spatial resolution is obtained by measuring the amplitude of the diffraction peak corresponding to the (011) atomic planes aligned with the tip apex. The Fourier calculation is performed on all the atoms in a small sphere of 1nm in radius centred on each atom successively. Assuming a Gaussian dispersion of atoms around their correct position (atomic plane position), it was demonstrated that the Fourier amplitude $\mathbf{|F(k_{011})|}$ depends on the spatial precision Δ_z. Using Δ_z the full width half maximum of the spatial precision in the real space, it was demonstrated that

$$\Delta_z \sim \frac{2d_{011}}{\pi}\sqrt{(\ln(2) \times \ln(\,|\mathbf{F}(\boldsymbol{k_{011}})|\,))} \qquad (11)$$

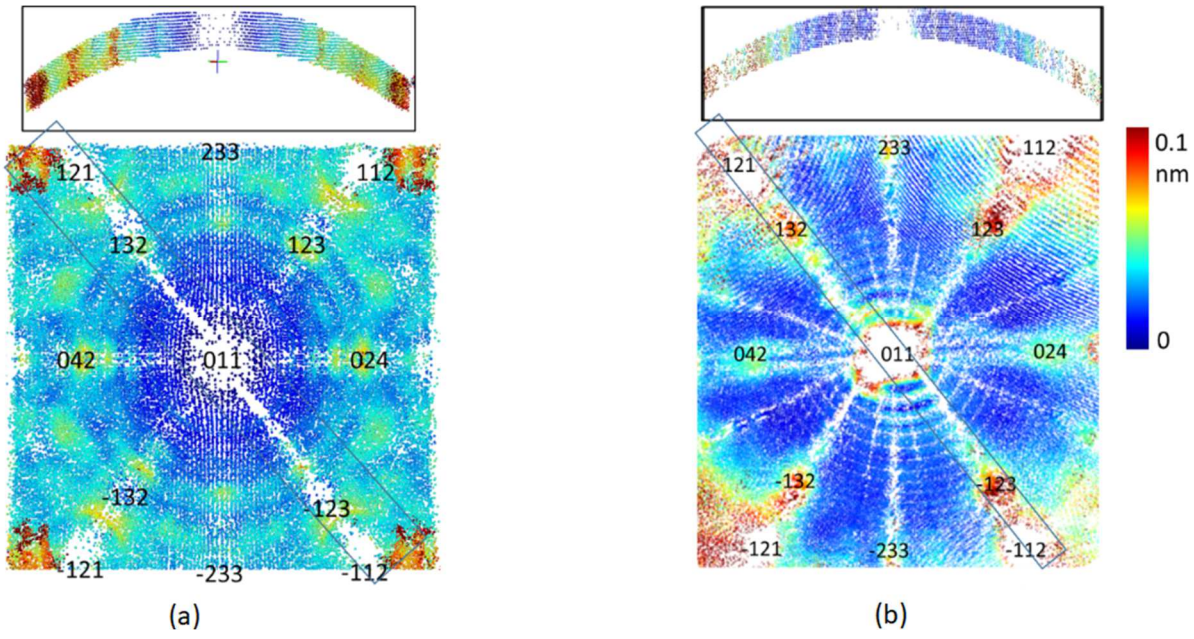

Figure 15 : *(a) Map of spatial resolution along [011] direction calculated on the 3DFIM tungsten simulation. Upper inset shows a slice in the reconstructed volume across the (011) pole. (b) Experimental map of spatial resolution along [011] direction calculated on the 3DFIM tungsten experiment (Blue spatial precision < 0.02 nm, Red thickness of atomic planes >0.1 nm). Upper inset shows a slice in the reconstructed volume across the (011) pole. Measurement was made on 10^5 reconstructed atoms*

Eq. 11 was used for experimental and simulated datasets (Fig.(15)) showing a similar behaviour. The best resolution is obtained when (011) atomic planes are parallel to the tip's surface with a minimum value of about 10pm in both experiment and simulation. A slight degradation of the resolution occurs with the distance to the centre of the pole. Indeed, the resolution along a given direction is the quadratic sum of the projection of the depth resolution and the projection of the lateral resolution along this particular direction, as observed experimentally in APT [53–55], albeit here with a much better lateral resolution for the FIM than the APT. We may note that (011) atomic planes are easily visible up to an angle of 40°. Some concentric variation of the resolution are also produced due to the ring distortion described previously. Some additional degradations of the resolution are observed close to pole centres, and in correlation with concentric rings artefacts. These degradations are probably related to the rapid evaporation of atoms on pole centres that may cause perturbation in the regular sequence of field evaporation.

4 Concluding remarks

We introduced a framework for the processing of field ion images and their reconstruction, and proposed a general model for simulating the imaging process in the field ion microscope. Unlike the old geometrical model usually used to provide an interpretation of images, this model integrates both the dynamic process of field evaporation considering classical field evaporation theory, and the process of field ionization near the specimen's surface, to reproduce the sequence of FIM images currently observed experimentally. This model is used to reproduce the imaging process of the last generation of 3DFIM. The atom-by-atom, gradual evolution of FIM images is found to have a significant effect on the projection law in the FIM, even if ions are emitted a few angstroms above the surface, at the critical distance of field ionization. Zones lines artefacts and slight distortions of the images are highlighted. Yet, we demonstrated that the spatial precision of the instrument can achieve 10pm, and the detection efficiency can achieve 100% in defined zones of the tip surface. This ability validates the possibility to achieve observation of very small crystallographic defects such as vacancy clusters. Note that this ability was used as early as in the 60's and 70's to directly image the early stages of radiation damage, manifesting as very small, atomic-scale defects in the crystal lattice. With the help of the modelling approach future works to interpret contrasts from various atomic scale features such as dislocations, dislocations loops, or small precipitates are now opened. This approach can be also further enhanced to give correct interpretations of contrasts generated when analysing simple alloys (binary or ternary). It will help the development of a future 3DFIM with analytic performances.

Acknowledgments

The work was funded through EMC3 Labex-FEDER DYNAMITE and the EQUIPEX ANR-11-EQPX-0020 (GENESIS).We also acknowledge the French platform METSA. Simulated samples were generated using the ATOMSK software [56]. Visualization was performed using OVITO software [57]. BG and SSK are grateful for the financial support the Max-Planck Gesellschaft via the Laplace project. BG acknowledges financial support from the ERC-CoG-SHINE-771602. FV thanks also the financial support of the University of Rouen through a CRCT funding and the Max-Planck-Institut für Eisenforschung GmbH for financial support during his research stay.

Bibliography

[1] Lefebvre-Ulrikson W 2016 *Atom probe tomography: put theory into practice* (London: Academic Press)

[2] Miller M K 2014 *Atom-probe tomography: the local electrode atom probe* (New York: Springer)

[3] Gault B 2012 *Atom probe microscopy* (New York: Springer)

[4] Müller E W and Bahadur K 1956 Field Ionization of Gases at a Metal Surface and the Resolution of the Field Ion Microscope *Phys. Rev.* **102** 624–31

[5] Muller E W 1965 Field Ion Microscopy *Science* **149** 591–601

[6] Chen Y C and Seidman D N 1971 On the atomic resolution of a field ion microscope *Surf. Sci.* **26** 61–84

[7] Speicher C A, Pimbley W T, Attardo M J, Galligan J M and Brenner S S 1966 Observation of vacancies in the field-ion microscope *Phys. Lett.* **23** 194–6

[8] Fortes M A, Smith D A and Ralph B 1968 The interpretation of field-ion micrographs: Contrast from perfect dislocation loops *Philos. Mag. J. Theor. Exp. Appl. Phys.* **17** 169–76

[9] Smith D A, Fortes M A, Kelly A and Ralph B 1968 Contrast from stacking faults and partial dislocations in the field-ion microscope *Philos. Mag. J. Theor. Exp. Appl. Phys.* **17** 1065–77

[10] Loberg B and Norden H 1973 Regular defect structures in high angle grain boundaries *Acta Metall.* **21** 213–8

[11] Seidman D N, Current M I, Pramanik D and Wei C-Y 1981 Direct observations of the primary state of radiation damage of ion-irradiated tungsten and platinum *Nucl. Instrum. Methods* **182–183** 477–81

[12] Beavan L A, Scanlan R M and Seidman D N 1971 The defect structure of depleted zones in irradiated tungsten *Acta Metall.* **19** 1339–50

[13] Stiller K and Andrén H-O 1982 Faulty field evaporation at di-vacancies in {222} tungsten *Surf. Sci. Lett.* **114** L57–61

[14] Schmid T E and Balluffi R W 1971 Formation and migration of artifact vacancies induced on gold surfaces by neon field ion microscopy *Surf. Sci.* **28** 32–44

[15] Katnagallu S, Nematollahi A, Dagan M, Moody M, Grabowski B, Gault B, Raabe D and Neugebauer J 2017 High Fidelity Reconstruction of Experimental Field Ion Microscopy Data by Atomic Relaxation Simulations *Microsc. Microanal.* **23** 642–3

[16] Dagan M, Gault B, Smith G D W, Bagot P A J and Moody M P 2017 Automated Atom-By-Atom Three-Dimensional (3D) Reconstruction of Field Ion Microscopy Data *Microsc. Microanal.* **23** 255–68

[17] Katnagallu S, Dagan M, Parviainen S, Nematollahi A, Grabowski B, Bagot P A J, Rolland N, Neugebauer J, Raabe D, Vurpillot F, Moody M P and Gault B 2018 Impact of local electrostatic field rearrangement on field ionization *J. Phys. Appl. Phys.* **51** 105601

[18] Moore A J W 1962 The structure of atomically smooth spherical surfaces *J. Phys. Chem. Solids* **23** 907–12

[19] Sanwald R C and Hren J J 1967 Computer simulation of field ion images *Surf. Sci.* **7** 197–204

[20] Gipson G S and Eaton H C 1980 The electric field distribution in the field ion microscope as a function of specimen shank *J. Appl. Phys.* **51** 5537

[21] M**?**ller E W 1951 Das Feldionenmikroskop *Z. F**?**r Phys.* **131** 136–42

[22] Beckey H D, Belcher R and Frieser H 2014 *Principles of Field Ionization and Field Desorption Mass Spectrometry: International Series in Analytical Chemistry.* (Kent: Elsevier Science)

[23] Gomer R 1961 *Field Emission and Field Ionization* (Cambridge: Havard University Press)

[24] Modinos A and Nicolaou N 1969 A generalized WKB method for calculating double barrier transmission coefficients *Surf. Sci.* **17** 359–71

[25] Rendulic K D 1971 Measurements on field adsorption of neon and helium and the field ionization of a helium-neon mixture *Surf. Sci.* **28** 285–98

[26] Rendulic K D 1973 On field adsorption, ionization rates and gas supply *Surf. Sci.* **34** 581–7

[27] Miller M K 1996 *Atom probe field ion microscopy* (Oxford : New York: Clarendon Press ; Oxford University Press)

[28] Tsukada M 1994 Theory of electron tunneling in scanning tunneling microscopy and field ion microscopy *Appl. Surf. Sci.* **76–77** 312–21

[29] Chang C-C, Hsiao J-Y and Hsieh C-P 2008 An Adaptive Median Filter for Image Denoising *2008 Second International Symposium on Intelligent Information Technology Application* 2008 Second International Symposium on Intelligent Information Technology Application (IITA) (Shanghai, China: IEEE) pp 346–50

[30] Bas P, Bostel A, Deconihout B and Blavette D 1995 A general protocol for the reconstruction of 3D atom probe data *Appl. Surf. Sci.* **87–88** 298–304

[31] Gault B, Haley D, de Geuser F, Moody M P, Marquis E A, Larson D J and Geiser B P 2011 Advances in the reconstruction of atom probe tomography data *Ultramicroscopy* **111** 448–57

[32] Vurpillot F 2001 *Étude de la fonction de transfert pointe-image de la sonde atomique tomographique* PhD thesis (Université de Rouen)

[33] De Geuser F and Gault B 2017 Reflections on the Projection of Ions in Atom Probe Tomography *Microsc. Microanal.* **23** 238–46

[34] Ceguerra A V, Day A C and Ringer S P 2019 Assessing the Spatial Accuracy of the Reconstruction in Atom Probe Tomography and a New Calibratable Adaptive Reconstruction *Microsc. Microanal.* **25** 309–19

[35] Larson D J, Gault B, Geiser B P, De Geuser F and Vurpillot F 2013 Atom probe tomography spatial reconstruction: Status and directions *Curr. Opin. Solid State Mater. Sci.* **17** 236–47

[36] Rolland N, Vurpillot F, Duguay S and Blavette D 2015 A Meshless Algorithm to Model Field Evaporation in Atom Probe Tomography *Microsc. Microanal.* **21** 1649–56

[37] Forbes R G and Chibane K 1986 DERIVATION OF AN ACTIVATION ENERGY FORMULA IN THE CONTEXT OF CHARGE DRAINING *J. Phys. Colloq.* **47** C7-65-C7-70

[38] Kreuzer H J, Nakamura K, Wierzbicki A, Fink H-W and Schmid H 1992 Theory of the point source electron microscope *Ultramicroscopy* **45** 381–403

[39] Sánchez * C G, lozovoi A Y and alavi A 2004 Field-evaporation from first-principles *Mol. Phys.* **102** 1045–55

[40] Ono T, Sasaki T, Otsuka J and Hirose K 2005 First-principles study on field evaporation of surface atoms from W(011) and Mo(011) surfaces *Surf. Sci.* **577** 42–6

[41] Barnes J and Hut P 1986 A hierarchical O(N log N) force-calculation algorithm *Nature* **324** 446–9

[42] Boll T and Al-Kassab T 2013 Interpretation of atom probe tomography data for the intermetallic TiAl+Nb by means of field evaporation simulation *Ultramicroscopy* **124** 1–5

[43] Vurpillot F, Gaillard A, Da Costa G and Deconihout B 2013 A model to predict image formation in Atom probeTomography *Ultramicroscopy* **132** 152–7

[44] Vurpillot F and Oberdorfer C 2015 Modeling Atom Probe Tomography: A review *Ultramicroscopy* **159** 202–16

[45] Gruber M, Vurpillot F, Bostel A and Deconihout B 2011 Field evaporation: A kinetic Monte Carlo approach on the influence of temperature *Surf. Sci.* **605** 2025–31

[46] Oberdorfer C 2014 *Numeric Simulation of Atom Probe Tomography* PhD thesis (Munster University)

[47] Oberdorfer C and Schmitz G 2011 On the Field Evaporation Behavior of Dielectric Materials in Three-Dimensional Atom Probe: A Numeric Simulation *Microsc. Microanal.* **17** 15–25

[48] Yao L, Withrow T, Restrepo O D, Windl W and Marquis E A 2015 Effects of the local structure dependence of evaporation fields on field evaporation behavior *Appl. Phys. Lett.* **107** 241602

[49] Ge X, Chen N, Zhang W and Zhu F 1999 Selective field evaporation in field-ion microscopy for ordered alloys *J. Appl. Phys.* **85** 3488–93

[50] Vurpillot F, Bostel A, Menand A and Blavette D 1999 Trajectories of field emitted ions in 3D atom-probe *Eur. Phys. J. - Appl. Phys.* **6** 217–21

[51] Waugh A R, Boyes E D and Southon M J 1976 Investigations of field evaporation with a field-desorption microscope *Surf. Sci.* **61** 109–42

[52] Vurpillot F, Danoix F, Gilbert M, Koelling S, Dagan M and Seidman D N 2017 True Atomic-Scale Imaging in Three Dimensions: A Review of the Rebirth of Field-Ion Microscopy *Microsc. Microanal.* **23** 210–20

[53] Cadel E, Vurpillot F, Lardé R, Duguay S and Deconihout B 2009 Depth resolution function of the laser assisted tomographic atom probe in the investigation of semiconductors *J. Appl. Phys.* **106** 044908

[54] Geiser B P, Kelly T F, Larson D J, Schneir J and Roberts J P 2007 Spatial Distribution Maps for Atom Probe Tomography *Microsc. Microanal.* **13** 437–47

[55] Moody M P, Gault B, Stephenson L T, Haley D and Ringer S P 2009 Qualification of the tomographic reconstruction in atom probe by advanced spatial distribution map techniques *Ultramicroscopy* **109** 815–24

[56] Hirel P 2015 *Atomsk: A tool for manipulating and converting atomic data files*

[57] Stukowski A 2010 Visualization and analysis of atomistic simulation data with OVITO–the Open Visualization Tool *Model. Simul. Mater. Sci. Eng.* **18** 015012